

Multi-channel modelling of the formation of vibrationally cold polar KRb molecules.

Svetlana Kotochigova¹, Eite Tiesinga², and Paul S. Julienne²

¹ *Department of Physics, Temple University, Philadelphia, PA 19122-6082, USA*

² *Joint Quantum Institute, NIST and University of Maryland, Gaithersburg, Maryland 20899-8423, USA.*

We describe the theoretical advances that influenced the experimental creation of vibrationally and translationally cold polar $^{40}\text{K}^{87}\text{Rb}$ molecules [1, 2]. Cold molecules were created from very-weakly bound molecules formed by magnetic field sweeps near a Feshbach resonance in collisions of ultra-cold ^{40}K and ^{87}Rb atoms. Our analysis include the multi-channel bound-state calculations of the hyperfine and Zeeman mixed $X^1\Sigma^+$ and $a^3\Sigma^+$ vibrational levels. We find excellent agreement with the hyperfine structure observed in experimental data. In addition, we studied the spin-orbit mixing in the intermediate state of the Raman transition. This allowed us to investigate its effect on the vibrationally-averaged transition dipole moment to the lowest ro-vibrational level of the $X^1\Sigma^+$ state. Finally, we obtained an estimate of the polarizability of the initial and final ro-vibrational states of the Raman transition near frequencies relevant for optical trapping of the molecules.

I. INTRODUCTION

The recent successful creation of a high phase-space-density gas of polar $^{40}\text{K}^{87}\text{Rb}$ molecules [1, 2] has been based on both new experimental and theoretical advances in manipulating and understanding properties of such molecules. This opens up the possibility of studying collective phenomena that rely on the long-range interactions between polar molecules. Future experiments can be envisioned in both weakly confining optical traps as well as optical lattices.

Our goal in this paper is to describe some of the theoretical advances that influenced the experimental creation of vibrationally and translationally cold polar $^{40}\text{K}^{87}\text{Rb}$ molecules. In particular, we theoretically analyze various factors that can affect this creation including the multi-channel description of the initial, intermediate, and final states of the formation by Raman transitions.

In a previous paper [3] we made the first steps towards obtaining practical guidelines for photoassociatively producing low v vibrational states of heteronuclear KRb. We calculated the electronic transition dipole moments between ground state of the KRb molecule and excited states. In addition, we obtained the permanent dipole moments of the polar $X^1\Sigma^+$ and $a^3\Sigma^+$ ground states. A relativistic electronic structure code was used.

In a second paper [4] we discussed the possibility of creating $X^1\Sigma^+$ molecules starting from doubly spin-polarized K and Rb atoms via two-photon photoassociation. We assumed that colliding atoms are initially in the doubly spin-polarized state, which only allows them to bond in the ground configuration $a^3\Sigma^+$ potential. We then found that there is a viable route from the doubly spin-polarized colliding atoms to the vibrationally ground $X^1\Sigma$ state

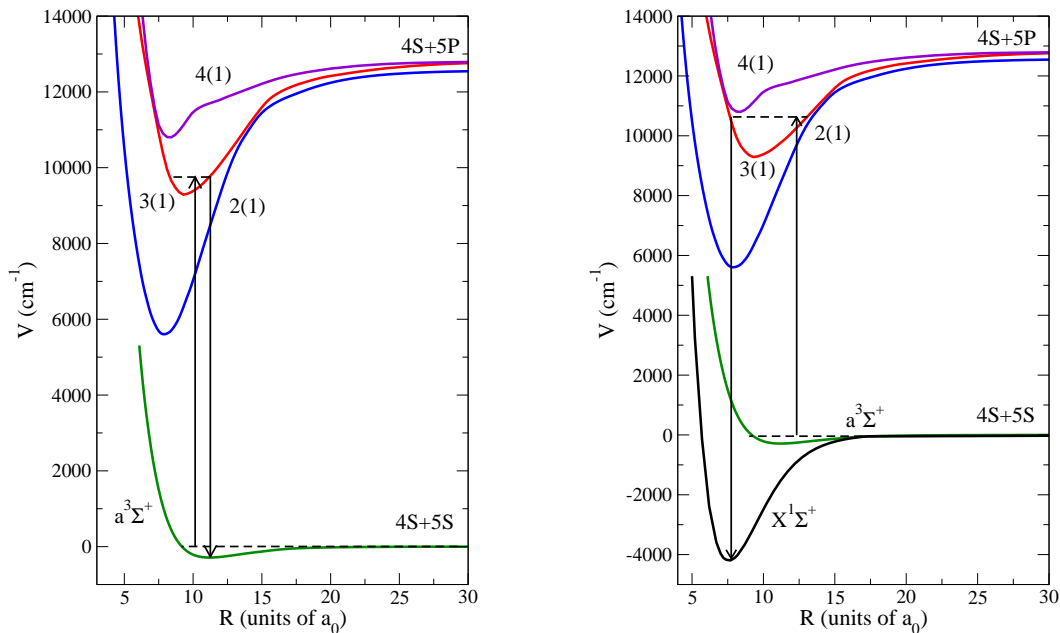


FIG. 1: The ground and excited state potential energy curves of KRb that are used for multi-channel modeling as a function of internuclear separation R . Here a_0 is the Bohr radius of 0.0529 nm.

via the excited $A^1\Sigma^+$ and $b^3\Pi$ states, when they are mixed through spin-orbit interactions. This mixing allows us to describe these potential by the Hund's case (c) coupling scheme as $2(0^+)$ and $3(0^+)$ states and calculate the Raman transition rate from the triplet state to the excited $\Omega = 0^+$ state followed by a downward transition to the ground singlet state. This process is absent in homonuclear dimers, since the additional *gerade-ungerade* symmetry prevents it. In the notation $m(\Omega)$ the number in parenthesis is the projection Ω of the total electronic angular momentum on the internuclear axis and the number in front labels the order of states with the same Ω . The role of black-body radiation in redistributing population among ro-vibrational levels of the singlet $X^1\Sigma^+$ and triplet $a^3\Sigma^+$ states was investigated.

Here we further search for an efficient production mechanism using a multi-channel description of both ground and excited states. We assume that KRb molecules are initially in the weakly-bound near-threshold vibrational states formed by a magnetic Feshbach resonance in collisions between ultracold ^{40}K and ^{87}Rb atoms. In our coupled-channel calculation of the ground state ro-vibrational structure we used the most accurate ground state potentials available from Ref. [5]. In section II we analyze this structure, and perform a comparison with available high-precision measurements [1, 2].

Vibrationally cold molecules are preferably made by transferring population from a Feshbach molecular state. For this transfer we selected the pathway that has been proposed by Stwalley [6], which forms vibrationally cold KRb molecules starting from the highly excited vibrational states using one optical Raman transition and intermediate vibrational levels of the $3(1)$ potential. This mechanism was also used to create vibrationally cold RbCs molecules in Ref. [7]. Reference [8] has reported an analysis of perturbations of the

vibrational levels of the 3(1) potential due to spin-orbit interactions with the neighboring potentials in RbCs.

For the vibrational levels used as intermediate states the 3(1) potential can to first order be described as the nonrelativistic $2^3\Sigma^+$ state. More accurately the strong non-adiabatic interaction with the neighboring 2(1) and 4(1) potentials has to be taken into account. Alternately, we can view this coupling as being due to the spin-orbit interaction between the nonrelativistic $2^3\Sigma^+$, $1^3\Pi$, and $1^1\Pi$ potentials. Therefore in Section III we perform multi-channel calculations of the ro-vibrational structure and the vibrationally-averaged transition dipole moments to the ground state levels. The three intermediate excited states that are of interest have $\Omega = 1$ symmetry and are shown in Fig. 1 together with the ground state potentials of KRb. In addition, panel a of Fig. 1 shows the pathway to form $v = 0$ $a^3\Sigma^+$ molecules starting from a gas of Feshbach molecules. Similarly, panel b shows the pathway to $v = 0$ $X^1\Sigma^+$ molecules.

The excited potentials in Fig. 1 were constructed from RKR data [9, 10] and as well as from our *ab initio* calculations. The two attractive 3(1) and 4(1) potentials dissociate to the $K(4s)+Rb(5p_{3/2})$ atomic limit whereas the 2(1) potential dissociates to the $K(4s)+Rb(5p_{1/2})$ limit. At short internuclear separations the potentials can be approximately described by the Hund's case (a) $n^{2S+1}\Lambda^\pm$ symmetry, where Λ is the projection of the electron orbital angular momentum along the internuclear axis and S is the total electron spin. At longer R relativistic effects are important, where the curves can only be described with Hund's case (c) $m(\Omega = 1)$ labeling.

In Section III our multi-channel calculation is, however, based on the nonrelativistic excited potentials $1^3\Pi$, $1^1\Pi$, and $2^3\Sigma$, electronic transition dipole moments to the ground states, and the spin-orbit coupling matrix elements. Some RKR data for the more deeply bound vibrational levels of the $1^1\Pi$ and $2^3\Sigma$ are available [9, 10]. We extend this information by *ab initio* electronic structure data and by known long range dispersion coefficients from Ref. [11].

The relativistic configuration interaction molecular orbital restricted active space (MOL-RAS-CI) method has been used to calculate potential energy curves, permanent and transition electric dipole moments of the KRb heteronuclear molecule as a function of internuclear separation. We combine this calculation with multi-channel ro-vibrational structure calculation to obtain Frank-Condon factors between the ground and excited states of KRb.

Finally, in Section IV we describe our calculation of the polarizability of vibrational levels of the $X^1\Sigma^+$ and $a^3\Sigma^+$ states.

II. COUPLED-CHANNEL CALCULATION OF THE GROUND STATES

In the Raman transition the initial and final bound vibrational levels belong to the ground $X^1\Sigma^+$ and $a^3\Sigma^+$ states. In KRb these states dissociate to the same $[Ar]4s(2S)+[Kr]5s(2S)$ atomic limit. The two states are coupled via hyperfine interactions: the Fermi-contact and electron and nuclear Zeeman interactions for each of the constituent atoms. For each atom the Fermi-contact interaction couples its electron spin, here 1/2, to its nuclear spin. The Zeeman interaction is non-zero since an external magnetic field is used to create Feshbach KRb molecules. The corresponding Hamiltonian for vibrational states in this coupled system has been discussed in Refs. [12, 13]. For this paper we include the effect of the weak magnetic dipole-dipole interaction perturbatively but do not include the effect of the second-order spin-orbit interaction [14].

Numerically solving for eigen pairs of this system is called a coupled-channel calculation. For our calculations we used the electronic potentials of Ref. [5]. The atomic masses for ^{40}K and ^{87}Rb are taken from Ref. [15], the Fermi-contact term values and electronic g-factors are from Ref. [16] and, finally, the nuclear magnetic moments are from Ref. [17]. The nuclear spin of ^{40}K is 4 and that of ^{87}Rb is 3/2.

The vibrational wave functions can be labeled by three nearly conserved angular momentum quantum numbers. These are the relative orbital angular momentum ℓ of the two atoms, its projection m_ℓ along the magnetic field direction, and the projection M_F of the summed atomic angular momentum $\vec{F} = \vec{f}_a + \vec{f}_b$ along the same direction. Here, \vec{f}_a and \vec{f}_b are total angular momenta of each atom. In fact, we can also write $\vec{F} = \vec{S} + \vec{I}$, where \vec{S} and \vec{I} are the total electron and nuclear spin, respectively.

For our calculations we neglect coupling between states with different $\ell m_\ell M_F$. In the absence of the magnetic dipole interaction the $2\ell + 1$ levels with the same ℓ and M_F quantum numbers are degenerate. For ultracold atoms and molecules we can limit ourselves to $\ell = 0$ and 2. As the Feshbach molecule created in [2, 18] has $\ell = 0$ and $M_F = -7/2$ we will limit ourselves to $M_F = -11/2$ to $-3/2$ as in a Raman transition M_F can change by upto two units depending on the polarization of the light beams.

Figure 2 shows the eigen energies and properties of eigen functions of a coupled-channel calculation with $M_F = -7/2$ and $\ell = 0$ at a magnetic field of $B=545.9$ G near the dissociation limit. The figure makes evident that mixing between the singlet $X^1\Sigma^+$ and triplet $a^3\Sigma^+$ states becomes strong within 150 GHz of the limit. The vertical axis shows the fraction of the $a^3\Sigma^+$ character in the wave function. A value close to zero (one) corresponds to a state primarily described as a $X^1\Sigma^+$ ($a^3\Sigma^+$) level. Our calculations finds non-degenerate hyperfine and Zeeman structure, which are grouped in Fig. 2 by a vibrational quantum number. Within each group there are twelve sublevels, which for weak mixing corresponds to three singlet and nine triplet sublevels. The vibrational quantum number is labeled according to the vibrational quantum number of the uncoupled singlet and triplet potential. The $v=-1$ level corresponds to the last uncoupled bound level. The grouping is valid in this case because the two potentials have the same long-range dispersion potential and sufficiently similar scattering lengths that the spacing between vibrational levels of the two potentials is nearly the same in the range of energy shown. For binding energies less than 3 GHz the levels with different vibrational quantum numbers intermix. The level relevant for the experiment of [2], which is the initial state of both Raman transitions in Fig. 1, is the most weakly bound sublevel with $M_F = -7/2$ and has a 0.23 MHz binding energy at $B=545.9$ G. Here, this state has 80 % $a^3\Sigma^+$ character. The weakly bound levels are now fully discussed in Ref. [19].

The final states of the Raman transitions are $v = 0$ levels of the $X^1\Sigma^+$ and $a^3\Sigma^+$ potentials. Figure 3 shows the rotational hyperfine and Zeeman structure of the $v = 0$ level of the $a^3\Sigma^+$ potential at $B=545.9$ G as calculated with the coupled-channel method. The black lines are the $\ell=0$ bound states and the red lines are the $\ell=2$ bound state. Notice though that the rotational energy splitting is smaller than that due to the hyperfine and Zeeman interaction. This leads to overlapping spectral features. The hyperfine structure of the two partial waves is nearly identical. The main difference is that each $\ell = 2$ hyperfine feature has within it three lines, which are not resolved in the figure. The splitting between these lines is less than 0.3 GHz and is due to the magnetic spin-spin dipole interaction, which partially lifts the m_ℓ degeneracy of the projection quantum number of $\vec{\ell}$.

The experiments of Refs. [1, 2] have located more than ten sublevels of the $v=0$ vibrational

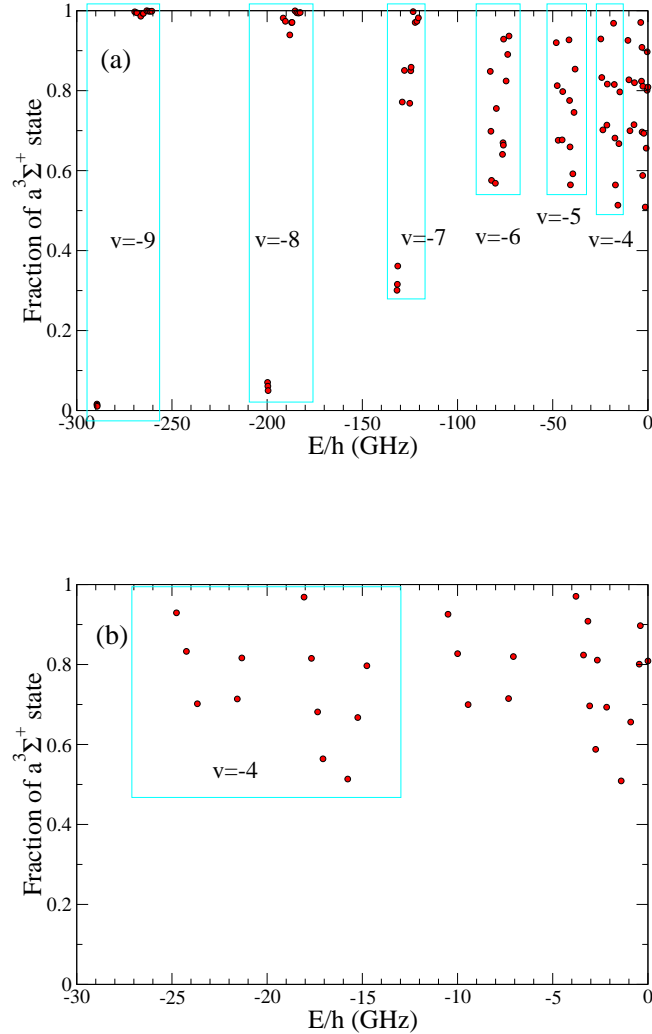


FIG. 2: Fraction of the $a^3\Sigma^+$ character of the coupled-channel eigen states of the $^{40}\text{K}^{87}\text{Rb}$ molecule as a function of their energy at a magnetic field of $B=545.9$ G. Bound states with $M_F = -7/2$ and $\ell = 0$ are shown. For energy between -300GHz and -15GHz the levels can be grouped by vibrational quantum number v of the uncoupled $X^1\Sigma^+$ and $a^3\Sigma^+$ potentials with $v = -1$ corresponding to the most weakly bound levels. Panel a displays vibrational levels from $v = -4$ to $v = -9$ and panel b is blowup of the near threshold region. Zero energy corresponds to the dissociation energy with both ^{40}K and ^{87}Rb in the energetically lowest hyperfine state.

level of the $a^3\Sigma^+$ potential. We have compared the calculated hyperfine structure of the $v=0$ level of the triplet state, shifted up by $+15.0$ GHz, with the experimental energies of Ref. [2], marked by the crosses and triangles in Fig. 3. The agreement is good.

Figure 4 shows the hyperfine and Zeeman structure of the $v=0$ vibrational state of the ground $X^1\Sigma^+$ state of $^{40}\text{K}^{87}\text{Rb}$ at $B=545.9$ G shifted up to $+0.4014$ GHz such that the energetically lowest $\ell = 0$ $M_F = -7/2$ level coincides with the experimental data indicated by triangles in Fig. 4. The two panel show energy levels for the lowest two even partial

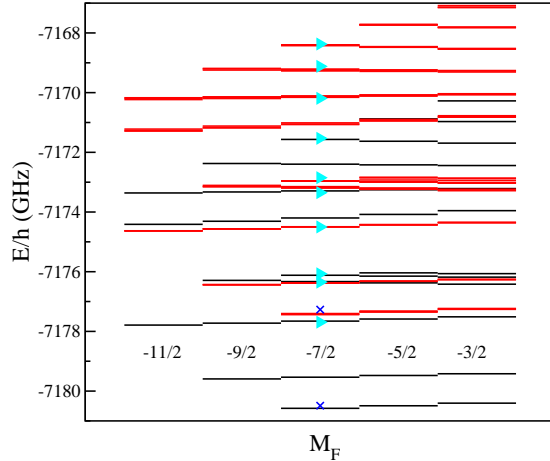


FIG. 3: The hyperfine and Zeeman structure at $B=545.9$ G of the $\ell=0$ (black lines) and 2 (red lines) rotational levels of the $v=0$ vibrational state of the $a^3\Sigma^+$ potential of $^{40}\text{K}^{87}\text{Rb}$. The crosses and triangles indicate the experimentally observed energies from Ref. [2]. The theoretical energies have been shifted up by $+15.0$ GHz to coincide with the experimental data. Zero energy corresponds to the dissociation energy of both ^{40}K and ^{87}Rb in the energetically lowest hyperfine state. The levels are grouped by the projection quantum number M_F . Each $\ell=2$ hyperfine feature contains three lines, which on the scale of the figure are barely resolved. The splitting is on the order of 0.1 GHz and due to the magnetic spin-spin dipole interaction, which partially lifts the m_ℓ degeneracy of the projection quantum number of $\vec{\ell}$.

waves. The singlet potential has to first order no hyperfine structure due to the Fermi contact interaction and electronic Zeeman interaction. Hence the structure in Fig. 4 is predominantly due to the nuclear Zeeman interaction of both atoms and is on the order of a few MHz at $B=545.9$ G. In fact, the nuclear Zeeman energy for the $X^1\Sigma^+$ state is given by

$$E_Z = -(g_{I,K}m_K + g_{I,Rb}m_{Rb})\mu_N B, \quad (1)$$

where m_K and m_{Rb} are the projections of the nuclear spin of ^{40}K and ^{87}Rb along the magnetic field direction, respectively. We then have $M_F = m_K + m_{Rb}$. The $g_{I,K}$ and $g_{I,Rb}$ are nuclear g-factors and μ_N is the nuclear magneton. The g-factor of K is about a factor of two smaller than that of Rb. In Fig. 4 each line can be labeled by m_K and m_{Rb} . The smaller splittings between lines correspond to levels with different m_K for the same m_{Rb} . The larger gaps between groups of levels correspond to different m_{Rb} . Each line of Fig. 4, panel b, contains five unresolved components corresponding to the five $\ell=2$ sublevels. Unlike the $\ell=2$ lines of the $a^3\Sigma^+$ state, the spin-spin dipole interaction here is zero to the first order and the second order contribution is very small.

For the $X^1\Sigma^+$ potential Ref. [2] has observed a single hyperfine component for the $\ell=0$ and 2 rotational state of the $v=0$ vibrational level. The experiment and theory agree to ≈ 401.4 MHz in an energy levels. The theoretical energy difference between $\ell=0$ and $\ell=2$ components of the $M_F = -7/2$ levels is 6.68376 GHz, which agrees well with the experimental value of $6.6836(5)$ GHz given in [2].

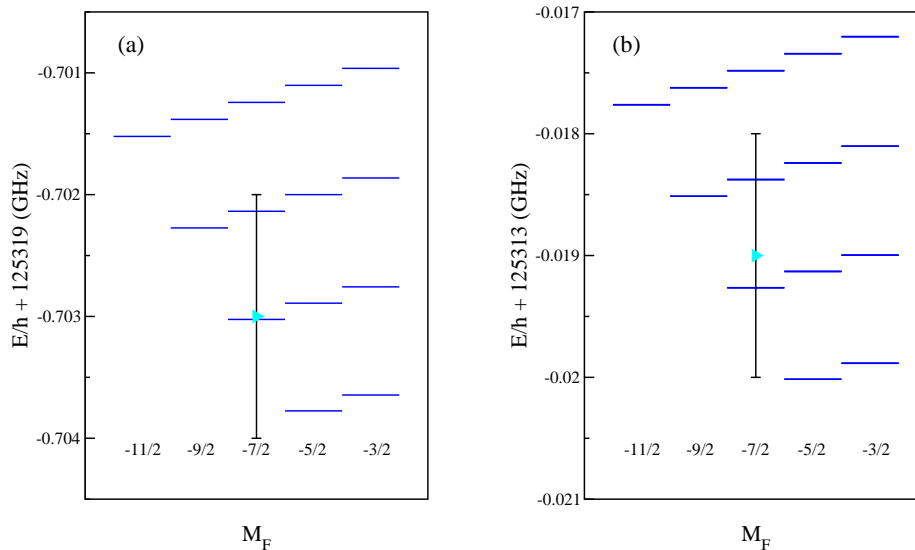


FIG. 4: The hyperfine and Zeeman structure of the $v=0$ $\ell=0$ level (panel *a*) and $\ell=2$ (panel *b*) of the $X^1\Sigma^+$ state of $^{40}\text{K}^{87}\text{Rb}$ at $B = 545.9$ G. The triangles with one-standard-deviation error bar indicate the experimentally observed energies from Ref. [2]. The theoretical energies have been shifted up by $+0.4014$ GHz such that the energetically lowest $\ell = 0$ $M_F = -7/2$ level coincides with the experimental data. The energy regions shown in the two panels are not the same. Zero energy corresponds to the dissociation energy of both ^{40}K and ^{87}Rb in the energetically lowest hyperfine state. The levels are grouped by the projection quantum number M_F .

III. MULTI-CHANNEL CALCULATION OF THE EXCITED STATES

In this section we model the ro-vibrational motion of the $^{40}\text{K}^{87}\text{Rb}$ molecule in excited electronic potentials, which are used as intermediates to create vibrationally cold molecules [2]. In particular, we focus on the need to use a multi-channel description of the vibrational structure that includes coupling between the electronic potentials. The origin of coupling can be explained from either the relativistic spin-orbit interaction, which couples non-relativistic $2S+1\Lambda^\pm$ Born-Oppenheimer (BO) potentials [20] or non-adiabatic mixing of relativistic Ω^\pm potentials. Some of the relativistic potentials as function of internuclear separation R are shown in Fig. 1. However, in this Section we first calculate multi-channel vibrational energies based on the non-relativistic potentials. We then discuss the effects of the multi-channel calculation on the vibrationally-averaged transition dipole moments. Due to the already complex nature of these calculations, we have not included the contributions of hyperfine, Zeeman, or coriolis interactions.

Note that as stated before for a non-relativistic potential the quantum number S , corresponding to the total electron spin \vec{S} , and Λ , corresponding the absolute value of the projection of the total electron orbital angular momentum, is conserved. For a relativistic calculation only Ω , the absolute value of the projection of the summed electronic orbital and spin angular momentum, are conserved. The \pm superscript, only relevant for $\Lambda = 0$ or $\Omega = 0$ states, distinguishing states with opposite reflection symmetries. For a given Ω symmetry nonrelativistic potentials that satisfy $-S \leq \Omega - \Lambda \leq S$, are coupled by spin-orbit

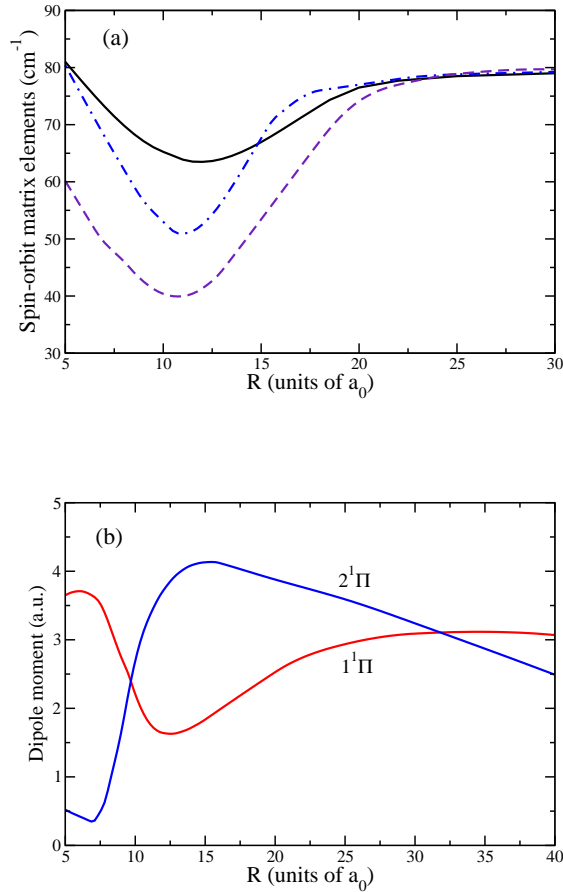


FIG. 5: Panel a: the R -dependent off-diagonal spin-orbit matrix elements between the $2^3\Sigma^+$ and $1^1\Pi$ potentials (solid line), the $2^3\Sigma^+$ and $1^3\Pi$ potentials (dashed line) and $1^1\Pi$ and $1^3\Pi$ potentials (dash-dotted line). For the spin-orbit interaction between $\Omega = 1$ potentials diagonal matrix elements are zero. Panel b: the R -dependent transition dipole moment between the $X^1\Sigma^+$ and two $1^1\Pi$ states. The dipole moments are in units of ea_0 , where e is the electron charge.

interactions. Strong mixing occurs when the energy splitting between $^{2S+1}\Lambda^\pm$ potentials is on the order of the spin-orbit interaction energy.

In our multi-channel calculation we use the $X^1\Sigma^+$ non-relativistic ground-state BO potential from Ref. [5] and the $2^3\Sigma^+$, $1^1\Pi$, and $1^3\Pi$ excited potentials from Ref. [21]. All three excited potentials dissociate to the $K(^2S)+Rb(^2P)$ limit. The previously unknown spin-orbit coupling matrix elements and electronic dipole moments are obtained from our MOL-RAS-CI calculations. The panel a in Fig. 5 shows the R -dependent spin-orbit matrix elements between the $2^3\Sigma^+$, $2^1\Pi$, and $1^3\Pi$ states. For the spin-orbit interaction between $\Omega=1$ potentials diagonal matrix elements are zero. As we will be interested in vibrational levels near the bottom of the $3(1)$ potential spin-orbit coupling to $2^1\Pi$ potential can be neglected. At large R the matrix elements approach $\Delta/3$, where Δ is the spin-orbit splitting of the 2P state of ^{87}Rb . The panel b in Fig. 5 shows the R -dependent transition dipole moment between the $X^1\Sigma^+$ and the $1^1\Pi$ and $2^1\Pi$ states. The dipole moments between the singlet

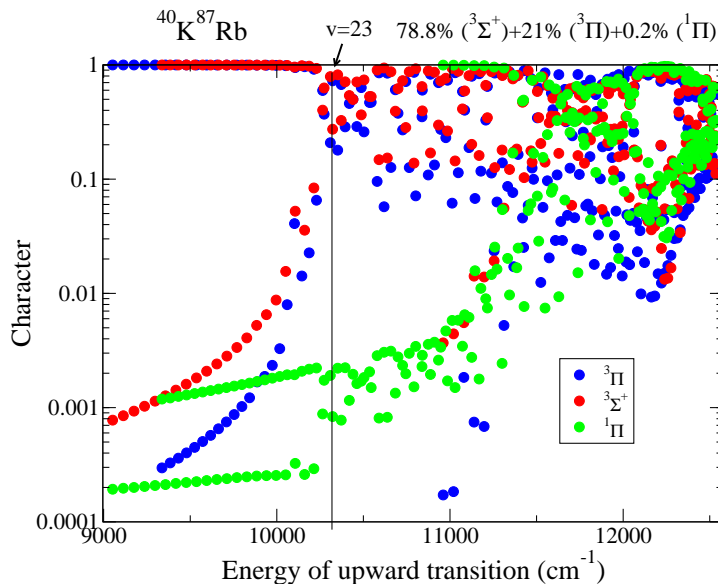


FIG. 6: The fraction of ${}^3\Pi$ (blue), ${}^3\Sigma^+$ (red), and ${}^1\Pi$ (green) character of the multi-channel $\Omega = 1$ eigen states of the ${}^{40}\text{K}{}^{87}\text{Rb}$ molecule as a function of energy. The level indicated by the label $v = 23$ corresponds to the $v=23$ bound state of the 3(1) potential used in [2]. Zero energy corresponds to the dissociation energy of both ${}^{40}\text{K}$ and ${}^{87}\text{Rb}$ in the energetically lowest hyperfine state. Hence the energy can be interpreted as the photon energy needed to make upward transition shown in the right panel of Fig. 1.

$X^1\Sigma^+$ and the triplet $2^3\Sigma^+$ and $1^3\Pi$ states are strictly zero.

Figure 6 shows the results of a multi-channel calculation of the vibrational levels of the $\Omega = 1$ excited states. We have coupled three channels, $2^3\Sigma^+$, $2^1\Pi$, and $1^3\Pi$, and, in addition, included the rotational potential $\hbar^2 J(J+1)/(2\mu R^2)$ with rotational quantum number $J = \Omega = 1$ to each channel. The vibrational energy on the horizontal axis is relative to the dissociation energy of ground state ${}^{40}\text{K}$ and ${}^{87}\text{Rb}$ and thus corresponds to the photon energy for the upward part of the Raman transition. Each vibrational level is represented by three circles, of different color but positioned at the same eigen energy, corresponding to the fraction of the three-channel wavefunction that is in the $2^3\Sigma^+$, $2^1\Pi$, and $1^3\Pi$ state, respectively. The sum of these fractions adds up to one. A level with a fraction one in a single channel corresponds to a vibrational level of an unperturbed $2^{S+1}\Lambda^\pm$ potential.

The energy range in Fig. 6 spans from just below the bottom of the 3(1) potential (See Fig. 1) to the atomic $\text{K}(2S)+\text{Rb}(2P_{3/2})$ limit. The $v = 0$ vibrational level of the 3(1) state can be identified at 9200 cm^{-1} . For energies $E > 9200 \text{ cm}^{-1}$ levels with a large fraction of ${}^3\Sigma^+$ character appear. For $E < 9200 \text{ cm}^{-1}$ only vibrational levels of the 2(1) or ${}^3\Pi$ state exist. Similarly at $E \approx 10900 \text{ cm}^{-1}$ eigen states with a large fraction in the ${}^1\Pi$ state appear. This corresponds to the bottom of the 4(1) potential. Interestingly, for all eigen states with energy $E < 10900 \text{ cm}^{-1}$ the levels have a small amount, < 0.01 , of ${}^1\Pi$ character. The 2(1) and 3(1) states have a small ${}^1\Pi$ admixture due to second-order spin-orbit mixing.

In other energy regions the characterization of levels is less clear. For example levels with energy larger than $E \approx 10200 \text{ cm}^{-1}$ have non-negligible contributions from the $2^3\Sigma^+$

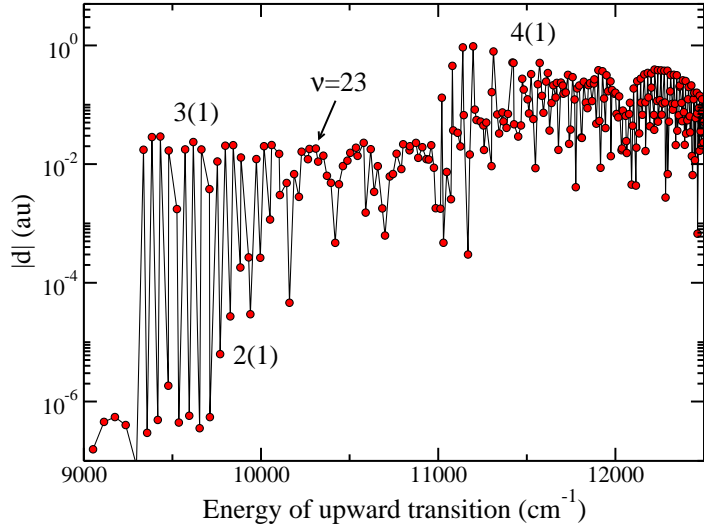


FIG. 7: Transition dipole moment from the $v=0$, $J=0$ $X^1\Sigma^+$ level to the excited $\Omega=1$ levels of the $^{40}\text{K}^{87}\text{Rb}$ molecule as a function of the excited-state energy. Zero energy corresponds to the dissociation energy of both ^{40}K and ^{87}Rb in the energetically lowest hyperfine state. The bound $v=23$ level of the 3(1) potential, used as intermediate state in [2], is marked. The calculated dipole moment to the $v=23$ level is 0.018 a.u.

and $^1\Pi$ states. These BO potentials of Ref. [21] cross at this energy and the spin-orbit interaction mixes the two symmetries. The intermediate vibrational level used in Ref. [2] and indicated by $v = 23$ in Fig. 6 is such a mixed state. From our calculation we find that it has a 79% $^3\Sigma^+$, 21% $^3\Pi$, and 0.2% $^1\Pi$ character. The closeness of the $v = 23$ level to the avoided crossing and the theoretical uncertainties in its location make the precise fractions uncertain. In fact, a few hundred cm^{-1} upward shift could potentially remove all $^3\Sigma^+$ and $^3\Pi$ mixing and the $v = 23$ level becomes a nearly pure $2^3\Sigma^+$ vibrational level. The $^1\Pi$ character, however, is not expected to change significantly.

Figure 7 shows the transition dipole moments between vibrational levels of the multi-channel $\Omega = 1$ calculation described above and the $v = 0$ $J = \ell = 0$ ro-vibrational level of the $X^1\Sigma^+$ potential assuming the electronic dipole moment shown in Fig. 5. This vibrationally-averaged dipole moment describes the downward part of the Raman transition. The energy region is as in Fig. 6 and the changing character of the excited state vibrational levels is reflected in the transition dipole moments. The vibrational averaged dipole moment from the singlet $X^1\Sigma^+$ state is only nonzero if the multi-channel vibrational levels contains $^1\Pi$ character. A larger character leads to a larger transition dipole moment. The start of the vibrational series of the 3(1) and 4(1) potential are clearly visible in the figure. The intermediate vibrational level used in Ref. [2] is again indicated by $v = 23$. From our calculation we find a dipole moment of 0.018 a.u. for the transition from this level.

IV. DYNAMIC POLARIZABILITY OF THE GROUND STATE VIBRATIONAL LEVELS

We examine the dynamic polarizability α of the KRb molecule as a function of laser frequency, ω , and ro-vibrational quantum numbers, v, J , of the uncoupled ground state $a^3\Sigma^+$ and $X^1\Sigma^+$ potentials. The real part of the dynamic polarizability, among other things, determines the depth of the trapping potential seen by a molecule as

$$V_0 = -\text{Re}(\alpha(\hbar\omega, v)) \times I, \quad (2)$$

where I is the intensity of the laser fields at frequency ω . The imaginary part of α describes the spontaneous or any other decay mechanism that leads to loss of molecules from the trap. Based on its knowledge, laser frequencies can be selected to minimize decoherence effects from loss of molecules due to spontaneous or laser-induced transitions.

The dynamic polarizability of a ro-vibrational level of the ground state is due to dipole coupling to all other ro-vibronic states of the ground and excited potentials. In contrast to the calculations in Sections II and III we do not include multi-channel effects due to either the hyperfine, Zeeman, or spin-orbit interaction. Instead, we base the calculation on our relativistic configuration-interaction MOL-RAS-CI determination of adiabatic $n(\Omega^\pm)$ potentials and relativistic transition dipole moments $d(R)$ between the ground- and excited states. The relativistic configuration-interaction theory treats the spin-orbit interaction non-perturbatively for the electronic wavefunction. Consequently, we use for the polarizability

$$\alpha(\hbar\omega) = \frac{1}{4\pi\epsilon_0} \frac{2\pi}{c} \sum_{\Omega' v' J' M'} |\langle \Omega' v' J' M' | d(R) \hat{R} \cdot \vec{\epsilon} | \Omega v J M \rangle|^2 \quad (3)$$

$$\times \left\{ \frac{1}{E_{\Omega' v' J'} - i\gamma_{\Omega' v' J'}/2 - (E_{\Omega v J} + \hbar\omega)} + \frac{1}{(E_{\Omega' v' J'} - i\gamma_{\Omega' v' J'}/2 + \hbar\omega) - E_{\Omega v J}} \right\}$$

where \hat{R} is the orientation of the interatomic axis, $|\Omega v J M\rangle$ and $|\Omega' v' J' M'\rangle$ are the ro-vibrational wavefunctions of initial Ω and final Ω' states, respectively. Here, M and M' are the projections of \vec{J} and \vec{J}' along a laboratory fixed axis. The vector $\vec{\epsilon}$ is the polarization of the laser, $E_{\Omega v J}$ is the ro-vibrational energy in the ground Ω state and $E_{\Omega' v' J'}$ is the ro-vibrational energy of the excited Ω' states. Contributions from scattering states or continuum of the excited Ω' states are also included. The widths $\gamma_{\Omega' v' J'}$ describe the spontaneous decay rate.

In our calculation of the polarizability dipole transitions to ro-vibrational levels within the $a^3\Sigma^+$ or $X^1\Sigma^+$ potentials as well as to ro-vibrational levels of excited $2(0^{+/-})$, $3(0^{+/-})$, $4(0^{+/-})$, $5(0^{+/-})$, $2(1)$, $3(1)$, $4(1)$, $5(1)$ and $6(1)$ potentials are included. The 0^- states do not contribute to the polarizability of the $X^1\Sigma^+$ ro-vibrational levels.

If a molecule is in a ro-vibrational level of the ground electronic potential and the frequency of a laser generated optical trap is nearly resonant to some molecular transition, this will lead to transfer of population to the ro-vibrational level of an excited potential, which then by the spontaneous emission can decay to many ro-vibrational levels of the ground potential. As result, we lose control over the molecule in the trap. To avoid this we must select trap frequency intervals in which resonant excitation is unlikely. We focus on the dynamic polarizability of the initial and final levels relevant to the Raman transition shown in the right panel of Fig. 1. Most experimentally used trapping laser use frequencies that

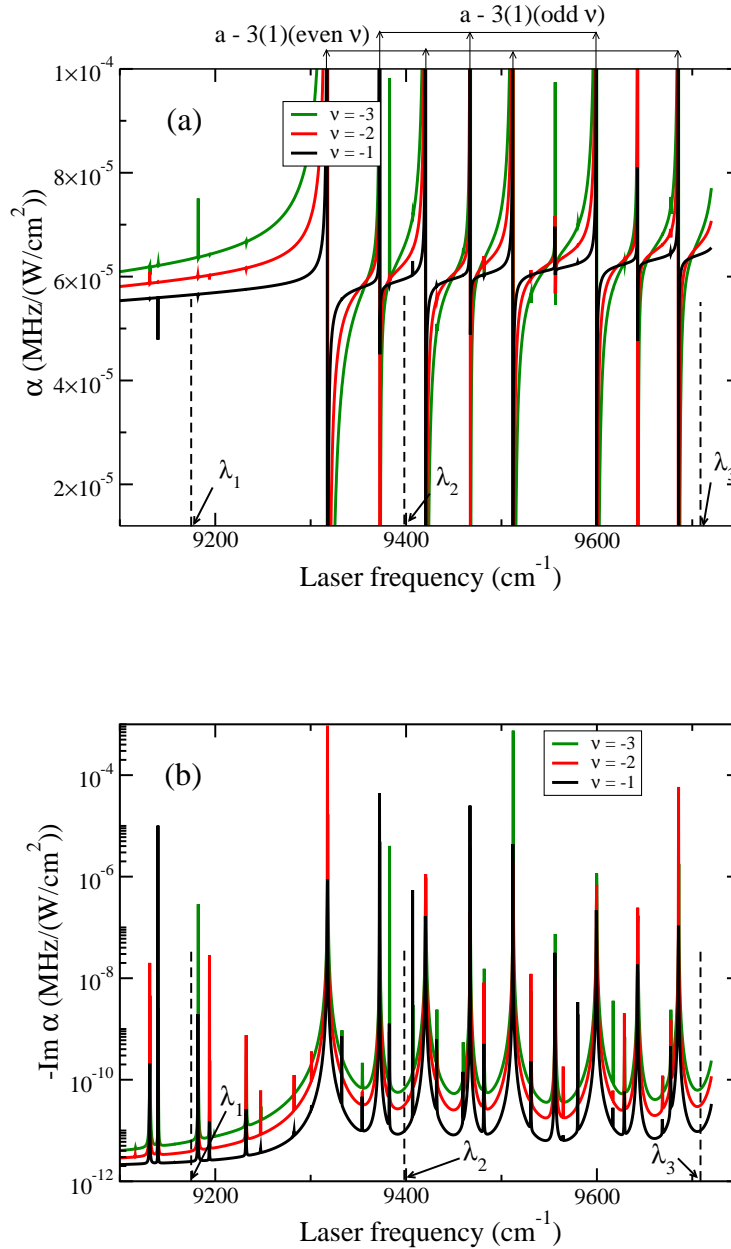


FIG. 8: Real (panel a) and minus the imaginary (panel b) part of the dynamic polarizability α of the $v=-1$, -2 , and -3 , $J=0$ ro-vibrational levels of the $a^3\Sigma^+$ ground state of KRb as a function of laser frequency. The most-widely-used trapping laser wavelengths, $\lambda_1 = 1090$ nm, $\lambda_2 = 1064$ nm, and $\lambda_3 = 1030$ nm, are indicated.

are located in the range between 9000 cm^{-1} and 9800 cm^{-1} . In particular, we examine the polarizability at laser wavelengths of 1090 nm, 1064 nm, and 1030 nm.

Figure 8 shows the real and imaginary part of the polarizability of the last three $J=0$ ro-vibrational levels ($v=-1, -2, -3$) of the $a^3\Sigma^+$ potential as a function of laser frequency. The polarizability has only been evaluated every 0.05 cm^{-1} . Most of the resonances in Fig. 8 are due to vibrational levels of the $3(1)$ potential. In the figure we have assigned the

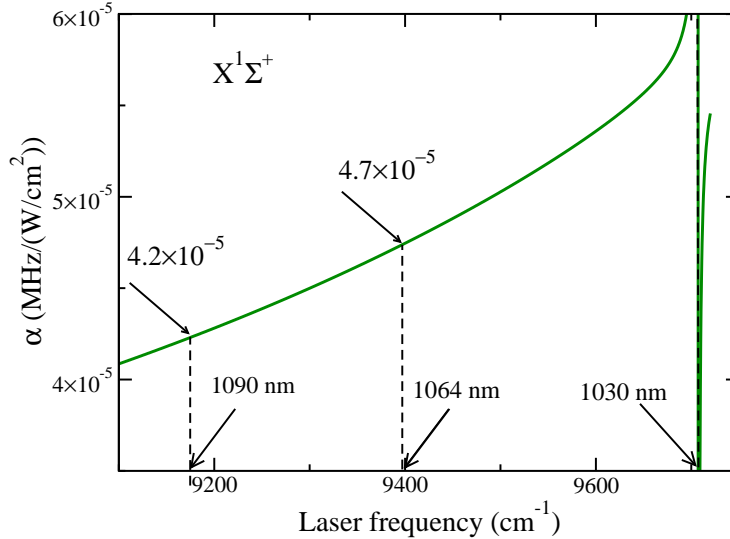


FIG. 9: Real part of the dynamic polarizability α of the $v=0$ $J=0$ level of the $X^1\Sigma^+$ ground state of KRb as a function of laser frequency within the range of 9100 cm^{-1} to 9710 cm^{-1} .

resonances due to transitions from the $v = -1$ level of the $a^3\Sigma^+$ potential to *even* or *odd* vibrational levels of the $3(1)$ excited potential. The even v levels have a stronger dipole moment and thus wider resonance. Away from the resonances the imaginary part of the polarizability is six to seven orders of magnitude smaller than the real part. This indicates that loss due to spontaneous emission from the excited state is negligible. We also indicate three trap wavelengths. As we can see from Fig. 8, the wavelength $\lambda_1 = 1090\text{ nm}$, used in the JILA experiments [1, 2], is far away from the resonances and has a very-small decoherence rate. The two other trap wavelengths, $\lambda_2 = 1064\text{ nm}$ and $\lambda_3 = 1030\text{ nm}$, lie around stronger resonances and their loss rate is predicted to be ten to hundred times larger.

Figure 9 shows the real part of the polarizability of the $v=0$ $J=0$ level of the $X^1\Sigma^+$ state of KRb as a function of laser frequency. Only one resonance is visible. It is due to the lowest ro-vibrational level of the excited $1^3\Pi(0^+)$ potential. This contribution to the polarizability is due to the spin-orbit mixing with the $2^1\Sigma(0^+)$ potential. The benchmark with the shortest wavelength lies very close to this resonance. However, the precise location of the resonance is unknown.

In summary, we performed a spin-coupling treatment that describes the hyperfine and Zeeman structure of the most weakly-bound and the most deeply-bound vibrational levels of the ground $X^1\Sigma^+$ and $a^3\Sigma^+$ potentials. The agreement with the observed experimental structures [2] is very good. Detailed structural understanding and assignment of the vibrationally-cold molecules is key for the coherent control of their interactions. In addition, we used a multi-channel description of the excited vibrational levels that includes R -dependent spin-orbit coupling between multiple non-relativistic $2^{S+1}\Lambda^\pm$ potentials. The spin-orbit coupling constants were obtained from an electronic structure calculation. Finally, we examined the dynamic polarizability α of vibrationally cold KRb molecules as a function of laser frequency ω . Based on this knowledge, laser frequencies can be selected to minimize

decoherence from loss of molecules due to spontaneous or laser-induced transitions.

V. ACKNOWLEDGMENT

SK acknowledges support from ARO and AFOSR and PSJ has partial support from ONR.

-
- [1] S. Ospelkaus, A. Peer, K.-K. Ni, J. J. Zirbel, B. Neyenhuis, S. Kotochigova, P. S. Julienne, J. Ye, and D. S. Jin, *Nature Physics* **4**, 622 (2008).
 - [2] K.-K. Ni, S. Ospelkaus, M. H. G. de Miranda, A. Peer, B. Neyenhuis, J. J. Zirbel, S. Kotochigova, P. S. Julienne, D. S. Jin, and J. Ye, *Science* **322**, 231 (2008).
 - [3] S. Kotochigova, P. S. Julienne, and E. Tiesinga, *Phys. Rev. A*, **68**, 022501(2003).
 - [4] S. Kotochigova, E. Tiesinga, and P. S. Julienne, *Eur. Phys. J. D* **31**, 189 (2004).
 - [5] A. Pashov, O. Docenko, M. Tamanis, R. Ferber, H. Knöckel, and E. Tiemann, *Phys. Rev. A* **76**, 022511 (2007).
 - [6] W. C. Stwalley, *Eur. Phys. J. D* **31**, 221225 (2004).
 - [7] J. Sage, S. Sainis, T. Bergeman, and D. DeMille, *Phys. Rev. Lett.* **94**, 203001 (2005).
 - [8] T. Bergeman, A. J. Kerman, J. Sage, S. Sainis, and D. DeMille, *Eur. Phys. J. D* **31**, 179 (2004).
 - [9] S. Kasahara, C. Fujiwara, N. Okada, and H. Katô, *J. Chem. Phys.* **111**, 8857 (1999).
 - [10] C. Amiot, *J. Mol. Spect.* **203**, 126 (2000).
 - [11] B. Bussery, Y. Achkar, and M. Aubert-Frèçon, *Chem. Phys.* **116**, 319 (1987).
 - [12] H. T. C. Stoof, J. M. V. A. Koelman, and B. J. Verhaar, *Phys. Rev. B* **38**, 4688 (1988).
 - [13] E. Wille, F. M. Spiegelhalder, G. Kerner, D. Naik, A. Trenkwalder, G. Hendl, F. Schreck, R. Grimm, T. G. Tiecke, J. T. M. Walraven, S. J. J. M. F. Kokkelmans, E. Tiesinga, and P. S. Julienne, *Phys. Rev. Lett.* **100**, 053201 (2007).
 - [14] F. H. Mies, C. J. Williams, P. S. Julienne, and M. Krauss, *J. Nat. Inst. Stand. Techn.* **101**, 521 (1996).
 - [15] G. Audi, A. H. Wapstra, and C. Thibault, *Nuclear Physics A* **729**, 337 (2003).
 - [16] E. Arimondo, M. Inguscio, and P. Violino, *Rev. Mod. Phys.* **49**, 31 (1977).
 - [17] N.J. Stone, Oxford University, preprint (2001) found at the website <http://ie.lbl.gov/toi.html>; P. Raghavan, *At. Data Nucl. Data Tables* **42**, 189 (1989).
 - [18] J. J. Zirbel, K.-K. Ni, S. Ospelkaus, T. L. Nicholson, M. L. Olsen, P. S. Julienne, C. E. Wieman, J. Ye, and D. S. Jin, *Phys. Rev. A* **78**, 013416 (2008).
 - [19] P. S. Julienne, arXiv:0812:1233.
 - [20] H. Lefebvre-Brion and R. W. Field, “*The spectra and dynamics of diatomic molecules*” Elsevier Academic Press, 2004.
 - [21] S. Rousseau, A. R. Allouche, and M. Aubert-Frèçon, *J. Mol. Spect.* **203**, 235 (2000).